

## Photocatalytic and thermoelectric performance of asymmetrical two-dimensional Janus aluminum chalcogenides

Haman, Zakaryae; Kibbou, Moussa; Khossossi, Nabil; Bahti, Soukaina; Dey, Poulumi; Essaoudi, Ismail; Ahuja, Rajeev; Ainane, Abdelmajid

**DOI**

[10.1088/2515-7655/ace07c](https://doi.org/10.1088/2515-7655/ace07c)

**Publication date**

2023

**Document Version**

Final published version

**Published in**

JPhys Energy

**Citation (APA)**

Haman, Z., Kibbou, M., Khossossi, N., Bahti, S., Dey, P., Essaoudi, I., Ahuja, R., & Ainane, A. (2023). Photocatalytic and thermoelectric performance of asymmetrical two-dimensional Janus aluminum chalcogenides. *JPhys Energy*, 5(3), Article 035008. <https://doi.org/10.1088/2515-7655/ace07c>

**Important note**

To cite this publication, please use the final published version (if applicable).  
Please check the document version above.

**Copyright**

Other than for strictly personal use, it is not permitted to download, forward or distribute the text or part of it, without the consent of the author(s) and/or copyright holder(s), unless the work is under an open content license such as Creative Commons.

**Takedown policy**

Please contact us and provide details if you believe this document breaches copyrights.  
We will remove access to the work immediately and investigate your claim.

PAPER • OPEN ACCESS

## Photocatalytic and thermoelectric performance of asymmetrical two-dimensional Janus aluminum chalcogenides

To cite this article: Zakaryae Haman *et al* 2023 *J. Phys. Energy* **5** 035008

View the [article online](#) for updates and enhancements.

### You may also like

- [Giant spin Hall effect in two-dimensional monochalcogenides](#)  
Jagoda Sawiska, Frank T Cerasoli, Haihang Wang *et al*.
- [Piezoelectricity in two-dimensional aluminum, boron and Janus aluminum-boron monochalcogenide monolayers](#)  
Saeed Choopani and Mustafa Menderes Alyörük
- [Piezo-phototronic solar cell based on 2D monochalcogenides materials](#)  
Gyan Michael, Gongwei Hu, Dongqi Zheng *et al*.



## PAPER

## OPEN ACCESS

## RECEIVED

16 March 2023

## REVISED

14 June 2023

## ACCEPTED FOR PUBLICATION

21 June 2023

## PUBLISHED

10 July 2023

Original Content from this work may be used under the terms of the [Creative Commons Attribution 4.0 licence](#).

Any further distribution of this work must maintain attribution to the author(s) and the title of the work, journal citation and DOI.



# Photocatalytic and thermoelectric performance of asymmetrical two-dimensional Janus aluminum chalcogenides

Zakaryae Haman<sup>1,\*</sup>, Moussa Kibbou<sup>1</sup>, Nabil Khossossi<sup>2,\*</sup> , Soukaina Bahti<sup>1</sup>, Poulumi Dey<sup>2</sup>, Ismail Essaoudi<sup>1</sup> , Rajeev Ahuja<sup>3,4</sup> and Abdelmajid Ainane<sup>1,\*</sup>

<sup>1</sup> Laboratoire de Physique des Matériaux et Modélisations des Systèmes, (LP2MS), Faculty of Sciences, Department of Physics, Moulay Ismail University, Meknes, Morocco

<sup>2</sup> Department of Materials Science and Engineering, Faculty of Mechanical, Maritime and Materials Engineering, Delft University of Technology, Mekelweg 2, 2628 CD Delft, The Netherlands

<sup>3</sup> Condensed Matter Theory Group, Materials Theory Division, Department of Physics and Astronomy, Uppsala University, Box 516, 75120 Uppsala, Sweden

<sup>4</sup> Department of Physics, Indian Institute of Technology Ropar, Rupnagar 140001, Punjab, India

\* Authors to whom any correspondence should be addressed.

E-mail: [zakaryae.haman@edu.umi.ac.ma](mailto:zakaryae.haman@edu.umi.ac.ma), [n.khossossi@tudelft.nl](mailto:n.khossossi@tudelft.nl) and [a.ainane@fs-umi.ac.ma](mailto:a.ainane@fs-umi.ac.ma)

**Keywords:** 2D materials, Janus Al-based monochalcogenides, electronic properties, optical properties, photocatalytic HER, thermoelectric properties

## Abstract

Through a density functional theory-driven survey, a comprehensive investigation of two-dimensional (2D) Janus aluminum-based monochalcogenides ( $\text{Al}_2\text{XY}$  with  $\text{X/Y} = \text{S, Se, and Te}$ ) has been performed within this study. To begin with, it is established that the examined phase, in which the Al-atoms are located at the two inner planes while the (S, Se, and Te)-atoms occupy the two outer planes in the unit cell, are energetically, mechanically, dynamically, and thermally stable. To address the electronic and optical properties, the hybrid function HSE06 has been employed. It is at first revealed that all three monolayers display a semiconducting nature with an indirect band gap ranging from 1.82 to 2.79 eV with a refractive index greater than 1.5, which implies that they would be transparent materials. Furthermore, the monolayers feature strong absorption spectra of around  $10^5 \text{ cm}^{-1}$  within the visible and ultraviolet regions, suggesting their potential use in optoelectronic devices. Concerning the photocatalytic performance, the conduction band-edge positions straddle the hydrogen evolution reaction redox level. Also, it is observed that the computed Gibbs free energy is around 1.15 eV, which is lower and comparable to some recently reported 2D-based Janus monolayers. Additionally, the thermoelectric properties are further investigated and found to offer a large thermal power as well as a high figure of merit (ZT) around 1.03. The aforementioned results strongly suggest that the 2D Janus Al-based monochalcogenide exhibits suitable characteristics as a potential material for high-performance optoelectronic and thermoelectric applications.

## 1. Introduction

Following the successful discovery and synthesis of single-layer graphene in 2004, a large number of two-dimensional (2D) materials have been synthesized experimentally and predicted computationally owing to their attractive chemical and physical properties as well as their versatile fields of application, such as thermoelectricity, optoelectronic and photocatalysis [1–5]. Most recently, a new family of 2D materials, known as the Janus phase, has been at the forefront of research owing to their inherent out-of-plane polarization and lack of mirror symmetry that differentiates them from other 2D monolayers counterparts [6–8]. With this background, the MoS<sub>2</sub> Janus monolayer was successfully synthesized through chemical vapor deposition using two distinct techniques: the selenization and sulfidation of the MoSe<sub>2</sub> and MoS<sub>2</sub> monolayers, respectively [9]. Accordingly, several publications have highlighted the potential and unique features of the Janus MoS<sub>2</sub> monolayer over their parental configurations. It has been also predicted that

Janus MXY (with M = Mo, W; X/Y = S, Se and Te with X ≠ Y) monolayers can serve as promising photocatalyst materials due to their appropriate electronic band gap, high carrier mobility, large-surface area, strong sunlight harvesting in the visible region and low-carrier recombination of electrons and holes [10–15]. Additionally, it has been revealed that Janus WSe possesses a low thermal conductivity compared to the pristine WS<sub>2</sub> and a high value of the figure of merit ZT, which makes the Janus WSe a potential candidate material for thermoelectric conversion [16, 17].

The search for 2D Janus monolayers has recently gained increasing attention, and several research efforts have been devoted to the design and exploration of new Janus phase structures. In particular, Janus monolayers based on group III monochalcogenides with the chemical formula MX (M = Al, Ga and In; X = S, Se, and Te) and a symmetry group P3m1 have been extensively investigated [12, 18]. 2D MX monolayers comprising four sub-layers, where the M-atoms are sandwiched between the X-atoms and can be converted into Janus phase through the substitution of Y-atoms at the top/bottom of the layers, yielding M<sub>2</sub>XY (M = Ga, In; X, Y = S, Se, Te) monolayers [15, 19–24]. Moreover, owing to the intrinsic dipole moment as well as the lack of mirror symmetry, these 2D monolayers were predicted theoretically to show superior potential application in fields of thermometric, piezoelectric, optoelectronic and photocatalysis [22, 25, 26].

Motivated by all the aforementioned insights regarding this new member in the family of 2D group-III metal monochalcogenides, we shall explore in this work different possibilities to implement 2D Janus aluminum monochalcogenide monolayers with the chemical formula Al<sub>2</sub>XY (X ≠ Y, X, Y = S, Se, Te) as a promising medium for optoelectronic, thermoelectric and photocatalytic applications. Within the framework of density functional theory (DFT) and Boltzmann transport equation, we fully optimized the three considered Janus monolayers and confirmed their dynamical, thermal, and mechanical stability through the finite displacement approach for the phonon dispersion, first-principle molecular dynamic (FPMD) simulations, and Young's modulus with Poisson's ratio, respectively. Also, the electronic properties along with the charge density differences, work function, and Bader charge analysis are performed based on two exchange-correlation functionals (i.e. GGA-PBE and HSE06). The optical performance features are further explored based on HSE06. The hydrogen evolution reaction (HER) activity in the presence and absence of a positive transverse electric field are also studied. Furthermore, the thermoelectric characteristics of the considered systems are systematically discussed. Our research offers an in-depth understanding of the physical behavior of 2D Janus aluminum monochalcogenide monolayers with respect to optoelectronic and thermoelectric applications as well as improved photocatalytic efficiency of these new 2D materials and also suggests appropriate guidelines for the realization and fabrication of advanced Al<sub>2</sub>XY-based monolayers.

## 2. Computational frameworks

### 2.1. Structural and electronic properties

All the calculations are performed based on DFT framework as implemented on the Vienna *Ab-initio* Simulation Package [27]. Generalized gradient approximation in the form of Perdew–Burke–Ernzerhof (GGA-PBE) [28] are used self consistently within the framework of the projector augmented wave through the plane wave basis ensemble along with an energy cutoff of 600 eV and the convergence criteria during the geometry optimizations were set to 10<sup>−6</sup> eV and 10<sup>−4</sup> eV Å<sup>−1</sup> for energy and force, respectively. In addition, to accurately understand the electronic behavior as well as derived accurate bandgap values, the Heyd–Scuseria–Ernzerhof (HSE-06) exchange-correlation hybrid functional was employed with a mixing constant of 25% [29]. During the geometry relaxations of all Janus structures, the vacuum was set to 20 Å along the *c*-direction to prevent the interaction between stacked layers and periodic pictures. The Monkhorst Pack K-point of the 24 × 24 × 1 grid was used in the reciprocal space during the geometrical optimizations [30]. The charge transfer is evaluated on the basis of the Bader charge algorithm [31]. The thermodynamic stability of the freestanding Janus structures is investigated, and the force constants are computed through the finite displacement method as implemented in Phonopy package [32–34] and the variation of the potential energy of large cell at 300 K in NVT scheme up to 10 ps through the FPMD simulations. More computational details can be found in our recent works [35, 36].

### 2.2. Optical properties

In addition, the optical properties of the three systems are reported, and the optical absorption spectra are derived directly through the imaginary part associated with the complex dielectric constant:

$$\epsilon = \text{Re}(\epsilon) + \text{Im}(\epsilon) \quad (1)$$

where  $\text{Re}(\epsilon)$  and  $\text{Im}(\epsilon)$  refer respectively to the real- and imaginary-part of the optical dielectric function [37–39]. On the other hand, the optical absorption spectra ( $\alpha(\omega)$ ) were computed based on the formula:

$$\alpha(\omega) = \sqrt{2}\omega \sqrt{|\epsilon(\omega)| - \epsilon_1(\omega)}, \quad (2)$$

where,

$$|\epsilon(\omega)| = \sqrt{[\epsilon_1^2(\omega) + \epsilon_2^2(\omega)]}. \quad (3)$$

The real and imaginary parts of the optical refractive index  $n(\omega)$  are explored based on the formula:

$$n(\omega) = \frac{1}{\sqrt{2}} \{ [\epsilon_1^2(\omega) + \epsilon_2^2(\omega)]^{1/2} + \epsilon_1(\omega) \}^{1/2}. \quad (4)$$

And, the electron energy loss function is given as follows:

$$L(\omega) = \frac{\epsilon_2(\omega)}{[\epsilon_1^2(\omega) + \epsilon_2^2(\omega)]}. \quad (5)$$

### 2.3. Thermoelectric transport properties

Additionally, the thermoelectric characteristics of the considered monolayers are investigated and described by the semi-classical Boltzmann transport theory in the context of the constant diffusion time and the rigid-band approaches. Initially, the transport distribution tensors through the electronic band structure is calculated using the formula below [40, 41]:

$$\sigma_{\alpha\beta}(\varepsilon) = \frac{e^2}{N} \sum_{i,k} \tau_{i,k} \nu_{\alpha}(i, k) \nu_{\beta}(i, k) \frac{\partial(\varepsilon - \varepsilon_{i,k})}{\partial \varepsilon}. \quad (6)$$

Therefore, one can derive other thermoelectric properties, namely, the Seebeck coefficient, the electrical conductivity, and the electronic thermal conductivity from the  $\sigma_{\alpha\beta}(\varepsilon)$  which can be further simplified as:

$$\sigma_{\alpha\beta}(\varepsilon) = \frac{1}{\Omega} \int \sigma_{\alpha\beta}(\epsilon) \left[ -\frac{\partial f_0(T, \epsilon, \mu)}{\partial \epsilon} \right] d\epsilon. \quad (7)$$

The Seebeck coefficient is given as follows:

$$S_{\alpha\beta}(T, \mu) = \frac{1}{eT\Omega\sigma_{\alpha\beta}(T, \mu)} \int \sigma_{\alpha\beta}(\varepsilon)(\varepsilon - \mu) \left[ -\frac{\partial f_0(T, \varepsilon, \mu)}{\partial \varepsilon} \right] d\varepsilon \quad (8)$$

and, the thermal electronic conductivity by:

$$\kappa_{\alpha\beta}^0(T, \mu) = \frac{1}{e^2 T \Omega} \int \sigma_{\alpha\beta}(\varepsilon)(\varepsilon - \mu)^2 \left[ -\frac{\partial f_0(T, \varepsilon, \mu)}{\partial \varepsilon} \right] d\varepsilon. \quad (9)$$

Herein,  $\alpha$ ,  $\beta$ , and  $e$  refer to the tensor indices and the charge of a single electron,  $N$  denotes the number of K-points mesh,  $\Omega$  denotes the primitive cell volume of  $\text{Al}_2\text{XY}$  monolayers,

Through our calculations, a constant optimization time was set to  $\tau = 10^{-14}$  s and several thermoelectric features such as electrical conductivity ( $\sigma/\tau$ ), thermal electronic conductivity ( $\kappa/\tau$ ), Seebeck coefficient (S), power factor (PF) as well as the figure of merit (ZT) were calculated at three temperatures (300, 600 and 900 K) with respect to the chemical potential  $\mu$ .

## 3. Results and discussion

### 3.1. Structural stability of 2D Janus $\text{Al}_2\text{XY}$ monolayers

The top and side views of fully optimized  $\text{Al}_2\text{XY}$  ( $X \neq Y$ ,  $X, Y = \text{S, Se, Te}$ ) monolayers are illustrated in figure 1 with the primitive unit-cell indicated by a dashed black hexagonal. Table 1 summarized the geometrical parameters including the lattice constants, thickness ( $h$ ), and bond length between the atoms Al–Al, Al–X/Y, and X–Y which are in good agreement with the previously published studies. The charge density difference with corresponding electron-charge transfer between Al- and (X/Y)-atoms in the case of 2D Janus  $\text{Al}_2\text{XY}$  ( $X \neq Y$ ,  $X, Y = \text{S, Se, Te}$ ) monolayers are studied as depicted in the figure 1 and the Bader charge are summarized in the table 2. One can distinctly observe a charge accumulation zone around (X/Y)-atoms and a depletion region around the Al atoms. A great electron-charge transfer is produced by the

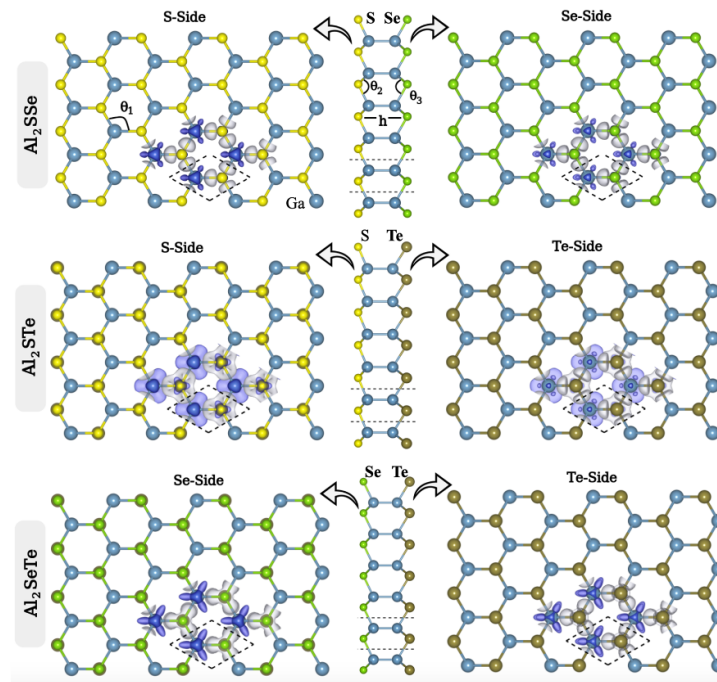


**Figure 1.** Geometrical structures of  $\text{Al}_2\text{XY}$  ( $X \neq Y$ ,  $Y = \text{S, Se, Te}$ ) monolayers with the primitive unit-cell indicated by a dashed black hexagonal. Difference charge density is indicated in the same panel. The gray and blue regions represent charge accumulation and depletion, respectively.

**Table 1.** Summary of geometrical and electronic properties of the three systems using GGA-PBE and HSE06, the lattice parameter ( $a$ ), bond lengths, thickness ( $h$ ), electronic bandgap ( $E_g$ ), and work function (WF).

Materials	$a = b$ (Å)	$d_{\text{Al-Al}}$ (Å)	$d_{\text{Al-X/Y}}$ (Å)	$d_{\text{Al-Y}}$ (Å)	$h$ (Å)	$E_g^{\text{PBE}}$ (eV)	$E_g^{\text{HSE06}}$ (eV)	WF (eV)
$\text{Al}_2\text{SSe}$	3.677	2.591	2.355	2.444	4.821	2.053	2.799	6.379
$\text{Al}_2\text{STe}$	3.853	2.580	2.413	2.631	4.919	1.182	1.823	5.314
$\text{Al}_2\text{SeTe}$	3.951	2.577	2.526	2.655	5.022	1.686	2.348	5.750

**Table 2.** The Bader charge transfer  $Q$  ( $|e|$ ) between Al and X in  $\text{Al}_2\text{XY}$  ( $X \neq Y$ ,  $Y = \text{S, Se, Te}$ ) monolayers.

Materials	$Q_{\text{Al}} e $	$Q_{\text{S}} e $	$Q_{\text{Se}} e $	$Q_{\text{Te}} e $
$\text{Al}_2\text{SSe}$	+1.371	−1.371	−1.371	—
$\text{Al}_2\text{STe}$	+0.808	−1.371	—	−1.371
$\text{Al}_2\text{SeTe}$	+0.650	—	−0.650	−0.650

strong electronegativity towards the weak electronegativity. Eventually, the work function ( $W$ ) is also investigated using the HSE06 functional and summarized in table 1 for the three 2D monolayers. Typically, the higher work function values imply the difficulty of an electron escaping from the surface of the monolayer. In this regard, it is expected that the 2D Janus  $\text{Al}_2\text{STe}$  material will provide a promising performance in terms of easy electron emission owing to its smallest work function of about 5.314 eV compared to  $\text{Al}_2\text{SSe}$  and  $\text{Al}_2\text{SeTe}$  monolayers. The Janus working functions are similar to the  $\text{C}_2\text{N}$  nanosheet (5.21 eV) [42] and the  $\text{MoS}_2$  monolayer (5.15 eV) [43], and higher than those of graphene (4.60 eV) [1] and the  $\text{InSe}$  monolayer (4.50 eV) [44].

Additionally, the phonon dispersion curve is studied to recheck the dynamical stability of the 2D Janus  $\text{Al}_2\text{SSe}$ ,  $\text{Al}_2\text{STe}$  and  $\text{Al}_2\text{SeTe}$  monolayers. The computed phonon dispersion curves are depicted in figures 2(a)–(c). One can clearly notice that the three systems present only the positive frequency mode without any negative mode in the entire Brillouin zone, which confirms the dynamical stability of the considered monolayers. Additionally, the *ab-initio* molecular dynamics simulations at 300 K for 10 ps were performed to confirm their thermal stability. Figures 2(d)–(f) shows the change in total energy and average force of all the three considered monolayers as a function of the time-steps for 2D Janus  $\text{Al}_2\text{SSe}$ ,  $\text{Al}_2\text{STe}$  and  $\text{Al}_2\text{SeTe}$  monolayers, respectively. It can be noticed that for the three systems, the fluctuations in energy and



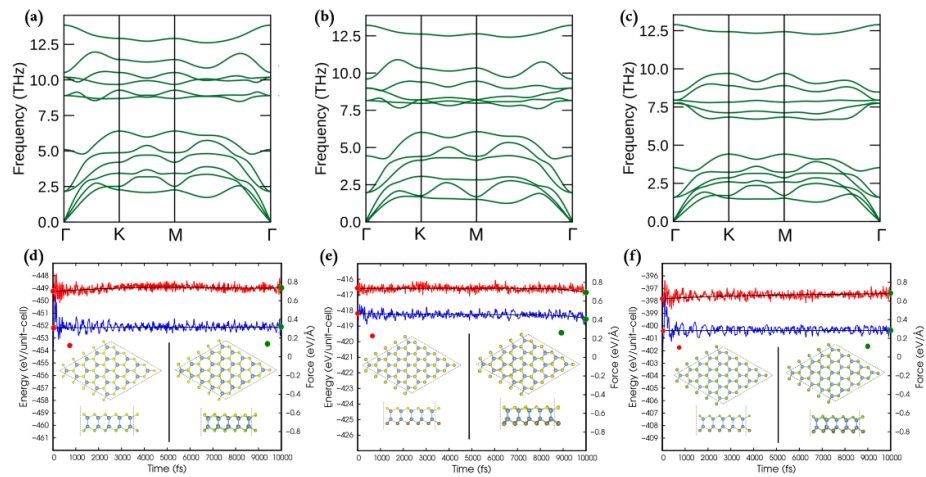


**Figure 2.** (a)–(c) Phonon dispersion spectra, (d)–(f) the fluctuation of total energy and average force at 300 K as a function of time for three considered 2D Janus  $\text{Al}_2\text{SSe}$ ,  $\text{Al}_2\text{STe}$  and  $\text{Al}_2\text{SeTe}$  monolayers, respectively. The inserts present the optimized structures before and after the different dynamic simulations.

**Table 3.** The calculated elastic stiffness constants (GPa) of the 2D Janus  $\text{Al}_2\text{XY}$  ( $X \neq Y$ ,  $X, Y = \text{S, Se, Te}$ ) monolayers.

Materials	$C_{11} = C_{22}$	$C_{12}$	$C_{44}$	$C_{66}$	$\nu$
$\text{Al}_2\text{SSe}$	42.105	11.267	15.397	0.040	0.230
$\text{Al}_2\text{STe}$	36.718	10.131	13.224	0.037	0.241
$\text{Al}_2\text{SeTe}$	34.744	9.419	12.635	0.025	0.240

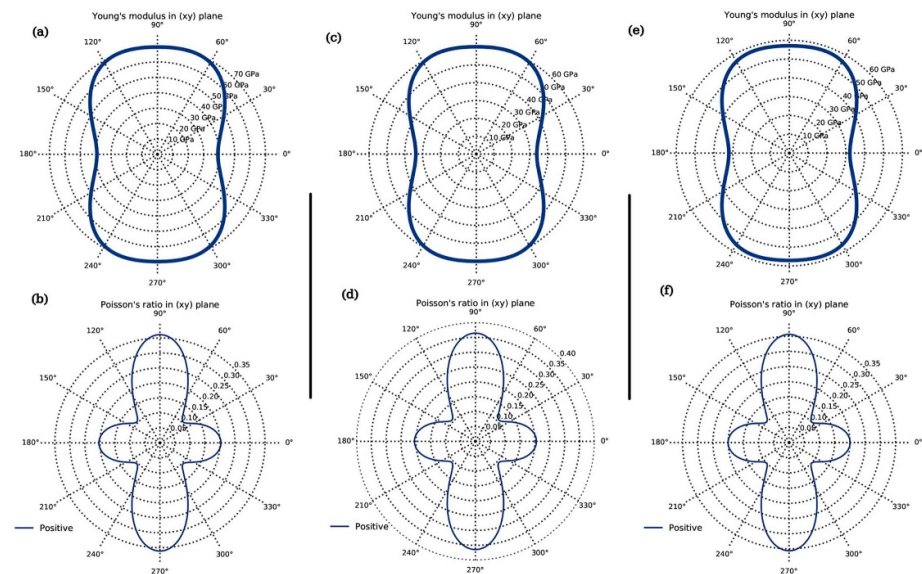


**Figure 3.** The computed mechanical properties of Young modulus and Poisson ratio of (a) and (b)  $\text{Al}_2\text{SSe}$ , (c) and (d)  $\text{Al}_2\text{STe}$  and (e) and (f)  $\text{Al}_2\text{SeTe}$  monolayers.

average force are very slight with no breaking of the Al–Al, Al–X/Y, and X–Y bonds which confirms the high degree of thermal stability.

Additionally, the mechanical properties were explored in order to check the flexibility of 2D Janus  $\text{Al}_2\text{SSe}$ ,  $\text{Al}_2\text{STe}$ , and  $\text{Al}_2\text{SeTe}$  monolayers. In this context, the elastic constants, the in-plane Young's modulus, and the Poisson ratio along different  $\theta$ -directions as a function of the positive  $x$ -direction were investigated. As listed in table 3, the computed elastic constants  $C_{11}$ ,  $C_{12}$ ,  $C_{44}$ , and  $C_{66}$ , suggest a strong bonding between the Al- and X/Y-atoms by satisfying the required conditions needed for good mechanical stability, namely  $C_{11} > 0$ ,  $C_{22} > 0$ ,  $C_{66} > 0$  and  $(C_{11}C_{22} - C_{12}^2 > 0)$  [45].

In order to gain a deeper understanding of mechanical properties, The in-plane Young's modulus  $E(\theta)$  and the Poisson's ratio  $\nu(\theta)$  were computed and illustrated in figure 3. The results show that in-plane Young's

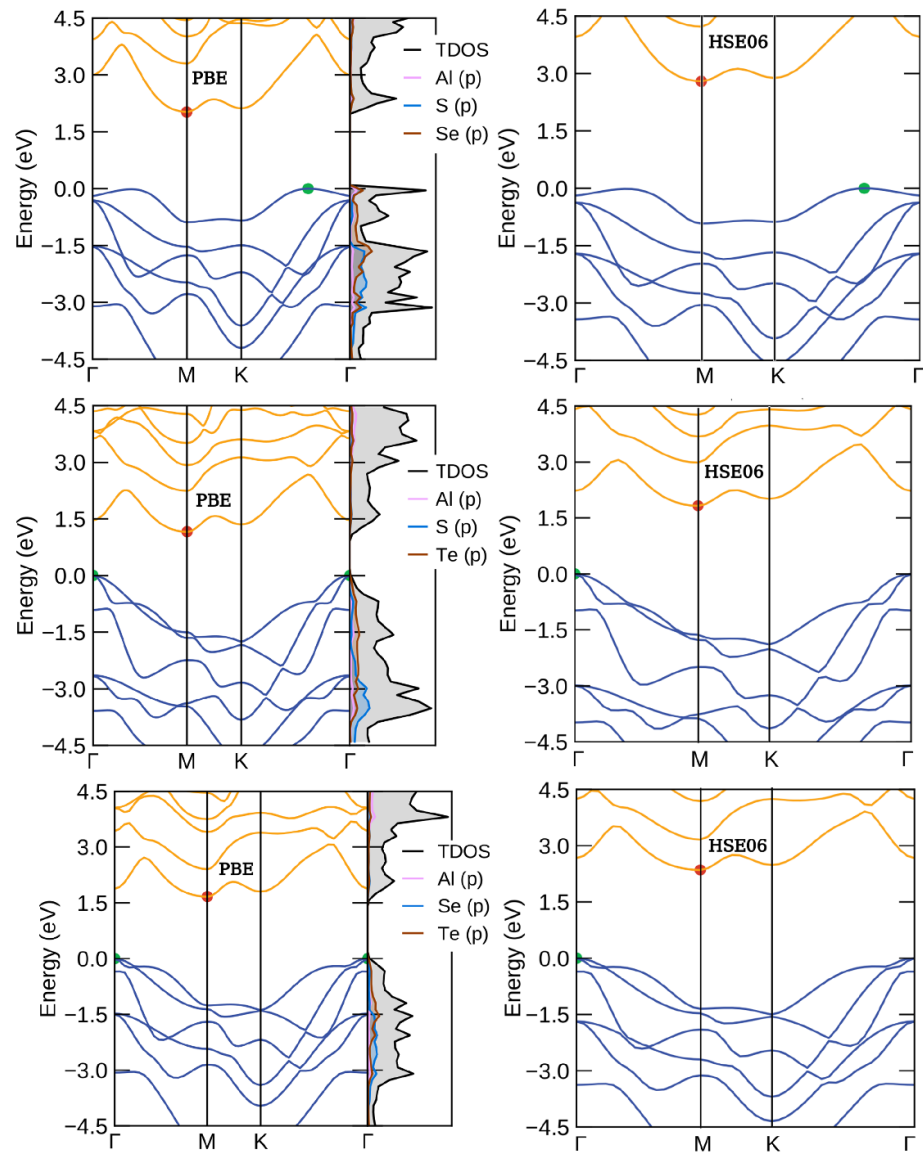


**Figure 4.** The computed electronic band structure, with corresponding total and projected density of state using PBE and HSE functionals for  $\text{Al}_2\text{SSe}$  (top figure),  $\text{Al}_2\text{STe}$  (middle figure), and  $\text{Al}_2\text{SeTe}$  (bottom figure) monolayers.

modulus of 2D Janus  $\text{Al}_2\text{XY}$  monolayers is highly an-isotropic (see figures 3(a), (c) and (e)). The maximum values of Young's modulus along  $x$ -directions are 264 GPa, 276 GPa, and 224 GPa for  $\text{Al}_2\text{SSe}$ ,  $\text{Al}_2\text{STe}$  and  $\text{Al}_2\text{SeTe}$  monolayer, respectively. whereas, its values along the  $y$ -directions are found to be 470 GPa, 500 GPa, and 400 GPa for  $\text{Al}_2\text{SSe}$ ,  $\text{Al}_2\text{STe}$  and  $\text{Al}_2\text{SeTe}$  monolayer, respectively. It was seen that the minimal and maximal Young's modulus of Janus monolayers are very close to each other. It is clear that Young's modulus of the considered 2D Janus monolayers is proportional to the atomic radius of X/Y-atoms. Compared to some other 2D materials, Young's modulus values of these three considered materials are smaller, e.g. compared to graphene monolayer which exhibits a maximum Young's modulus values equal to 1000 GPa [46]. Furthermore, all the considered 2D Janus monolayers present only positive Poisson's ratio along the  $45^\circ$  and  $135^\circ$  as along  $x$ - and  $y$ -directions. The maximal Poisson ratios are 0.13, 0.168, and 0.22 along the  $y$ -direction while in the  $x$ -direction, its values are relatively low i.e. 0.07, 0.092, and 0.12 for  $\text{Al}_2\text{SSe}$ ,  $\text{Al}_2\text{STe}$  and  $\text{Al}_2\text{SeTe}$  monolayers, respectively.

### 3.2. Electronic properties and band alignments of 2D Janus $\text{Al}_2\text{XY}$ monolayers

#### 3.2.1. Electronic properties

In order to understand the behaviors of the 2D Janus  $\text{Al}_2\text{XY}$  ( $X \neq Y$ ,  $Y = \text{S}, \text{Se}, \text{Te}$ ) monolayers, the electronic properties through the band structure and density of state were investigated by means of both exchange-correlation PBE and HSE-06 functional. Figure 4 displays the electronic band structures for the three considered monolayers, It can be clearly observed that all the 2D Janus  $\text{Al}_2\text{SSe}$ ,  $\text{Al}_2\text{STe}$ , and  $\text{Al}_2\text{SeTe}$



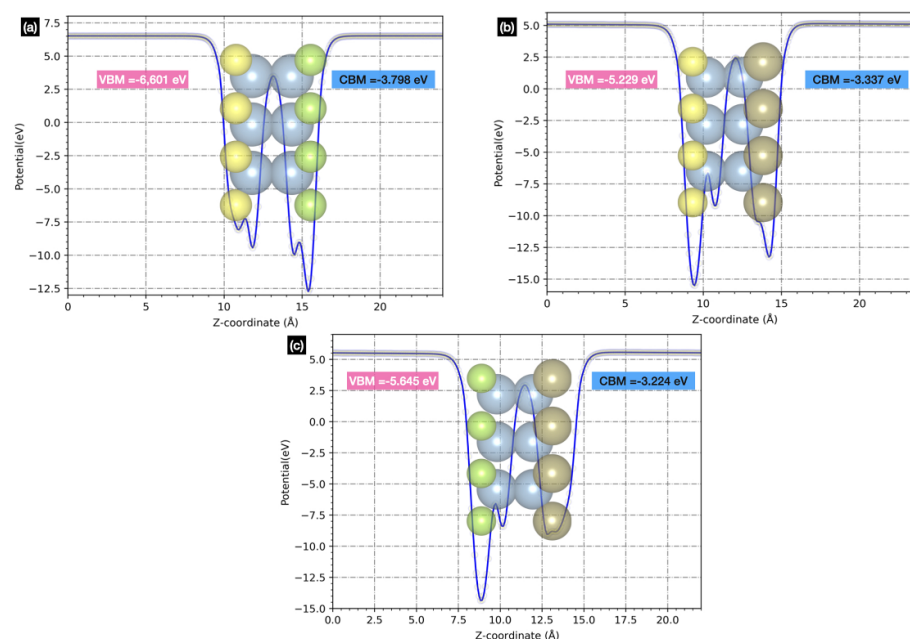


**Figure 5.** Electrostatic potentials and the band edge positions for (a) Al<sub>2</sub>SSe, (b) Al<sub>2</sub>STe, (c) Al<sub>2</sub>SeTe along the Z-direction.

monolayers exhibit a semiconducting nature with indirect band-gaps which is in line with recently reported studies. The computed electronic band gaps through PBE/HSE06 are 2.053/2.799, 1.182/1.823, and 1.686/2.348 eV for the Al<sub>2</sub>SSe, Al<sub>2</sub>STe, and Al<sub>2</sub>SeTe monolayers, respectively (see table 1). It can be clearly confirmed that the band gap energy of our monolayers is intricately linked to the atomic radius, which is in good agreement with previous work [15]. atomic radius is from these findings. Also, the conduction band minimum (CBM) for the three considered Janus monolayers are located in the M-point of the Brillouin-zone, and the valence band maximum (VBM) moves from the K- $\Gamma$  valley to the  $\Gamma$ -point with respect of the atomic-radius of (S, Se, Te)-atoms. Similar trend has been observed in the case of 2D Al-chalcogenides AlX (X = O, S, Se, and Te) monolayers [25]. To get a deeper insight into the contribution of electronic states in both VBM and CBM, the total and projected density of states were computed as shown in figure 4 for 2D Janus Al<sub>2</sub>SSe, Al<sub>2</sub>STe, and Al<sub>2</sub>SeTe monolayers. For the three considered systems, a great contribution from p-Al and p-(X/Y) orbitals on the valence band, while a relatively slight contribution from the p-(X/Y) orbitals on the conduction band.

### 3.2.2. Band alignments

Apart from the band gaps, band edge alignment is another condition for water redox reactions. In this case, the CBM must be more than  $-4.44$  eV (which is the hydrogen reduction potential of  $H^+/H_2$ ), while the VBM must be less than  $-5.67$  eV (the water oxidation potential of  $O_2/H_2O$ ). To get an in-depth overview, the band edges of Al<sub>2</sub>SSe, Al<sub>2</sub>STe, and Al<sub>2</sub>SeTe were aligned to the vacuum levels in order to identify the thermodynamic possibilities for water splitting and oxidation that each system possesses at both pH = 0 and pH = 7.

Since Janus structures lack vertical mirror symmetry, electric dipoles are created by charge transfer between their top and bottom surfaces. The consequence is that the vacuum levels on each side have unequal energies as shown in figure 5. In particular, the Janus structures have the potential to overcome the band gap limitations of traditional photocatalysts by allowing for a shift in the alignment of water splitting potentials with regard to the locations of their band edges. As a result of calculation of the electrostatic potentials and band structures, we find the VBM and CBM locations for Al<sub>2</sub>SSe, Al<sub>2</sub>STe, and Al<sub>2</sub>SeTe,  $-6.601$  and  $-3.798$  eV,  $-5.229$  and  $-3.337$  eV, and  $-5.645$  and  $-3.224$  eV, respectively. Based on figure 6, all three of these monolayers have CBM locations greater than  $-4.44$  eV at both pH = 0 and pH = 7, suggesting they may act as promising photocatalysts for hydrogen production via water splitting.

### 3.3. Optical properties

The optical response of materials to light is an essential feature in photocatalytic activity. Here, we explore the light-gathering characteristics of the considered Janus monolayers. The frequency-dependent complex dielectric function is utilized to obtain various optical parameters, including absorption coefficient, and

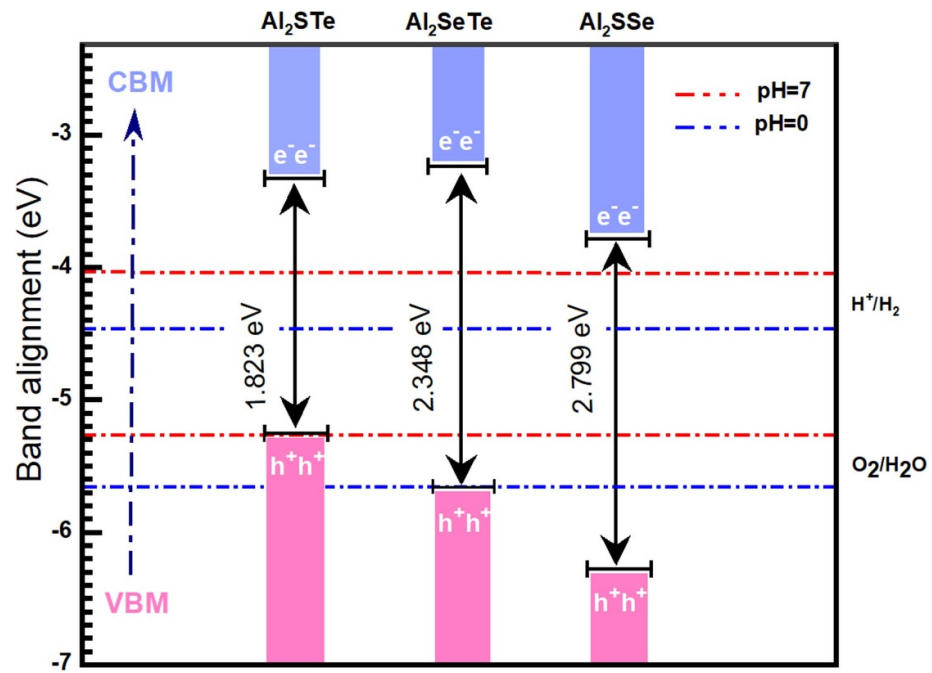


Figure 6. Calculated conduction and valence band-edge position of 2D Janus  $\text{Al}_2\text{XY}$  ( $\text{X} \neq \text{Y}$ ,  $\text{Y} = \text{S}, \text{Se}, \text{Te}$ ) monolayers.

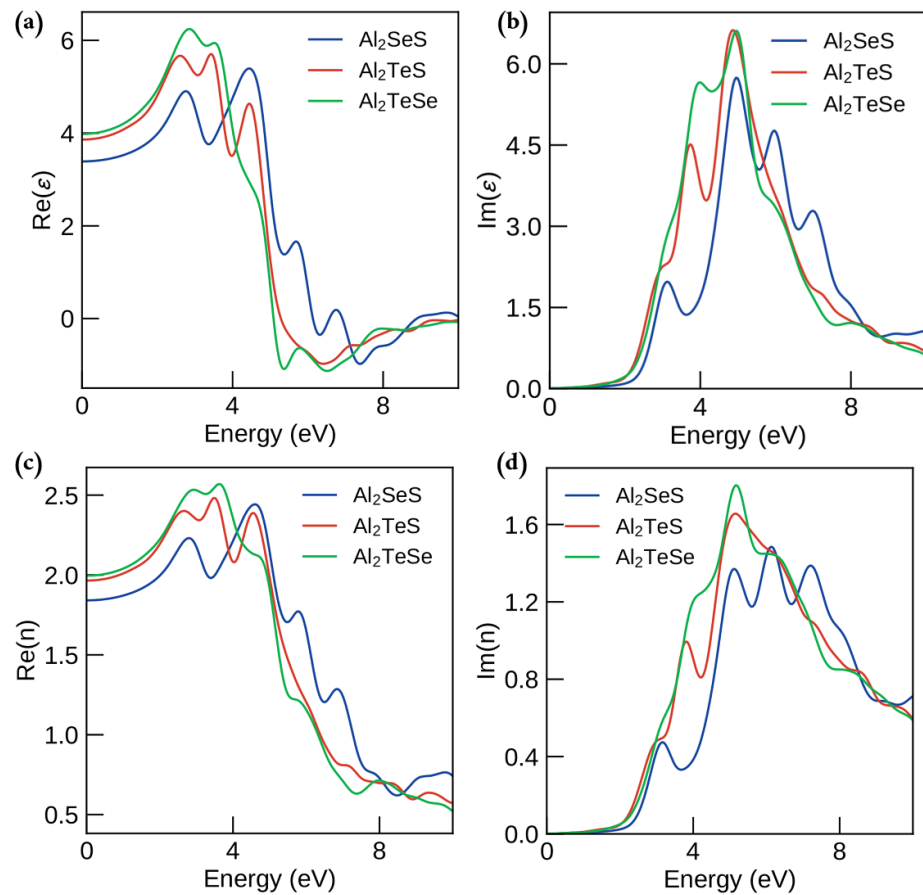
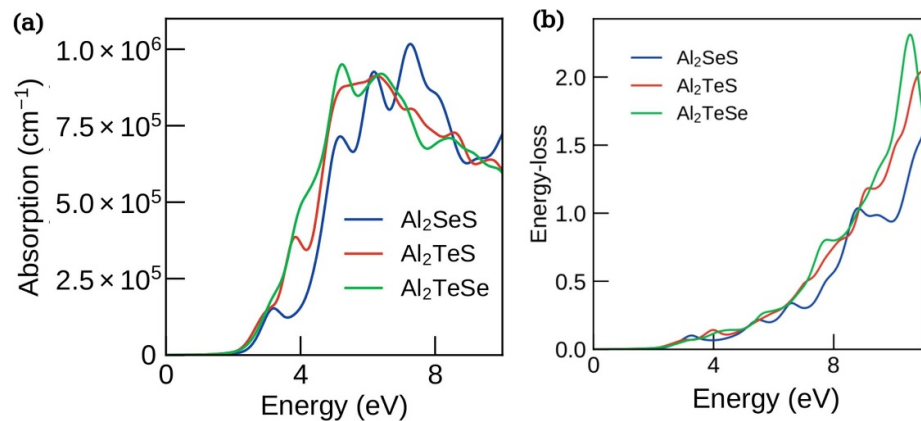


Figure 7. The comparisons of (a), (b) real and imaginary parts of the complex dielectric function, (c), (d) real and imaginary part of the complex refractive index of  $\text{Al}_2\text{SSe}$ ,  $\text{Al}_2\text{STe}$ , and  $\text{Al}_2\text{SeTe}$  monolayers.



**Figure 8.** The comparisons of (a) absorption spectra and (b) electron-energy loss function of  $\text{Al}_2\text{SeS}$ ,  $\text{Al}_2\text{TeS}$ , and  $\text{Al}_2\text{SeTe}$  monolayers obtained using the HSE06 hybrid functional.

energy loss function. The dielectric constant in both parts (imaginary and real) versus photon energy is shown in figures 7(a) and (b). The estimated static dielectric constant of Janus monolayers  $\text{Al}_2\text{SeS}$ ,  $\text{Al}_2\text{TeS}$ , and  $\text{Al}_2\text{SeTe}$ , which occur at zero photon energy, are respectively 3.5, 4.0, and 4.1, which indicate the high electronic polarizability of these Janus monolayers. Nevertheless, the static dielectric functions are well comparable to that of Janus  $\text{Al}_2\text{OS}$  reported recently [3]. Additionally, the first peaks of the imaginary part appear in the visible region at 3 eV, 3.5 and 3.8 eV for Janus  $\text{Al}_2\text{SeS}$ ,  $\text{Al}_2\text{TeS}$ , and  $\text{Al}_2\text{SeTe}$ , respectively. The studied Janus monolayers were evaluated for their light-harvesting performance, by calculating the absorption coefficient spectrum, which describes how light decays over a unit distance in an absorbing material and loss function. In figures 8(a) and (b), it can be clearly seen that the absorption coefficient spectrum presents many peaks within the considered energy level. Since we are interested in the visible-water splitting photocatalytic activity, the studied Janus monolayers have significant light harvesting in the visible region, particularly around 3 eV and the absorption values reach over  $1.5 \times 10^5 \text{ cm}^{-1}$ . Similar trends were obtained in the case of 2D Janus  $\text{Ga}_2\text{SSe}$ ,  $\text{Ga}_2\text{STe}$ , and  $\text{Ga}_2\text{SeTe}$  monolayers [47] and 2D Janus transition metal oxides MXO ( $M = \text{Ti, Hf and Zr}$ ;  $X = \text{S and Se}$ ) monolayers [48].

In a solid, electrons can be activated by absorbing photons, which carry energy. Additionally, when a high-speed electron moves within a medium, it can transfer energy to other electrons, leading to their excitation. Furthermore, electron excitation in solids can occur collectively, not just individually. This collective excitation can be detected by analyzing the energy loss spectrum  $L(\omega)$ , which is related to the inverse of the imaginary dielectric function. In the case of intraband and interband transitions,  $L(\omega)$  can reveal plasmonic excitations. The higher peak in the  $L(\omega)$  spectrum indicates the feature related to plasma resonance, and the corresponding higher frequency represents the plasma frequency to which the electrons can respond. Further, one can notice from a close examination of the electron energy-loss function that Janus monolayers  $\text{Al}_2\text{SSe}$ ,  $\text{Al}_2\text{STe}$ , and  $\text{Al}_2\text{SeTe}$  show important peaks. As shown in figure 8(b), the maximum peaks of the studied monolayers are located at high energy, as the loss function occurs in the UV region.

The real and imaginary parts of the complex refractive index for the three systems under consideration were calculated with respect to photon energy, and the results are plotted in figures 7(c) and (d). It can be clearly noticed that the static refractive index values are 1.8, 2, and 2.1 eV for the  $\text{Al}_2\text{SSe}$ ,  $\text{Al}_2\text{STe}$ , and  $\text{Al}_2\text{SeTe}$  monolayers, respectively.

### 3.4. Photocatalytic activity of 2D Janus $\text{Al}_2\text{XY}$ monolayer

The production of hydrogen by means of the photocatalytic water splitting method has proven to be a significant alternative to tackle cost and resource issues related to new hydrogen production approaches. In this regard, in order to further develop our understanding of the HER process, the binding energy of a single hydrogen atom on the surface of the materials can provide perhaps the clearest indicator of the HER performance of a variety of catalysts [25, 49]. The adsorption energy for a single hydrogen-atom adsorbed on  $\text{Al}_2\text{XY}$  ( $X \neq Y$ ;  $X, Y = \text{S, Se, Te}$ ) monolayers is given by the following formula:

$$\Delta E_{\text{H}^*} = E_{\text{Al}_2\text{XY}+\text{H}} - E_{\text{Al}_2\text{XY}} - \frac{1}{2}E_{\text{H}_2}, \quad (X \neq Y | X, Y = \text{S, Se, Te}) \quad (10)$$

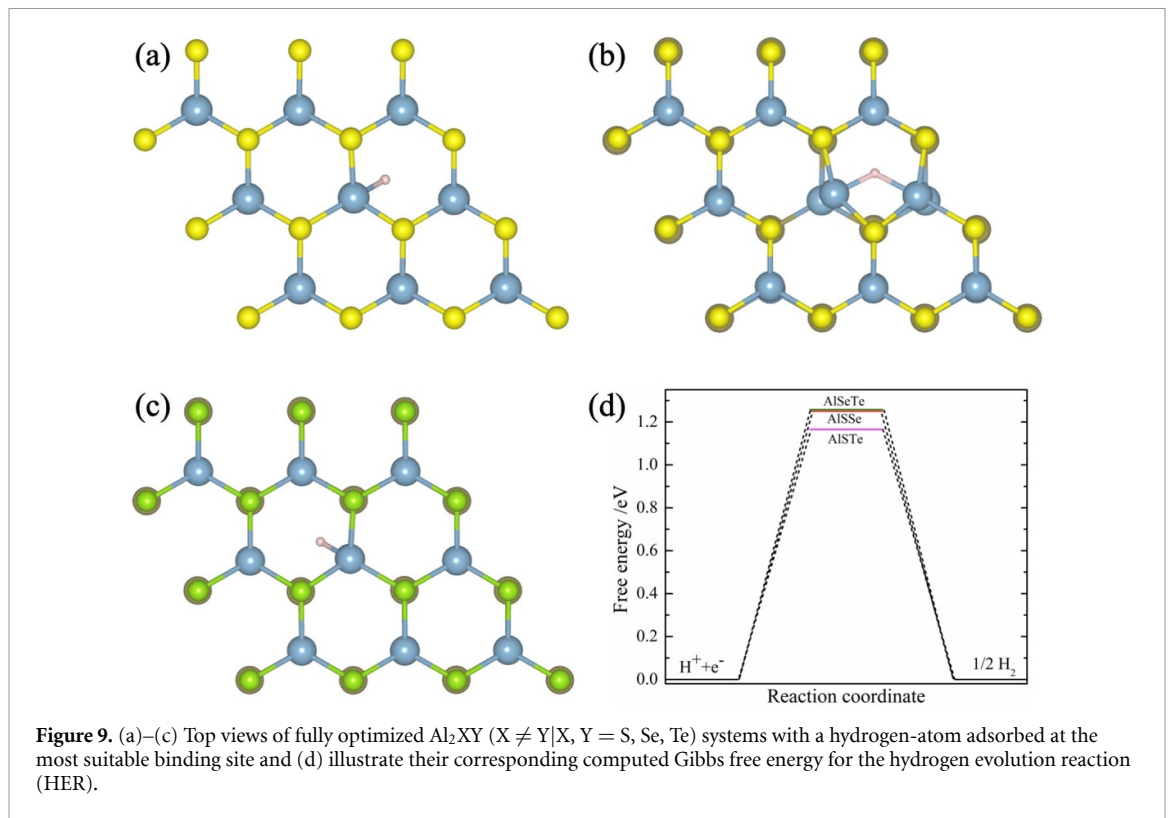


**Figure 9.** (a)–(c) Top views of fully optimized Al<sub>2</sub>XY (X ≠ Y|X, Y = S, Se, Te) systems with a hydrogen-atom adsorbed at the most suitable binding site and (d) illustrate their corresponding computed Gibbs free energy for the hydrogen evolution reaction (HER).

in which,  $E_{\text{Al}_2\text{XY}+\text{H}}$  and  $E_{\text{Al}_2\text{XY}}$  refers to the total energy of Al<sub>2</sub>XY monolayers after and before the adsorption of single hydrogen-atom, respectively, while the  $E_{\text{H}_2}$  refer to the total energy of H<sub>2</sub>-molecule.

The HER catalytic activity for the three considered materials is computed based on the hydrogen adsorption Gibbs free energy that is yielded through the formula:

$$\Delta G_{\text{H}^*} = \Delta E_{\text{H}^*} - T\Delta S_{\text{H}} + \Delta E_{\text{ZPE}} \quad (11)$$

where  $\Delta E_{\text{H}^*}$ ,  $\Delta S_{\text{H}}$ , and  $\Delta E_{\text{ZPE}}$  denotes the hydrogen adsorption energy, the variation of H<sub>2</sub>-molecule entropy between the adsorbed and gas-phase system, and the change in zero-point energy, respectively. The Al<sub>2</sub>XY (X ≠ Y|X, Y = S, Se, Te) monolayers yield a relatively insignificant contribution towards  $\Delta S_{\text{H}}$  and  $\Delta E_{\text{ZPE}}$ . Thus,  $\Delta S_{\text{H}} = -\frac{1}{2}S_{\text{H}_2}$ , with  $S_{\text{H}_2}$  denote the H<sub>2</sub>-molecule entropy at ambient conditions in its gas-reference state. Additionally, the term  $T\Delta S_{\text{H}}$  is approximately equal to  $-0.21$  eV. As a result, the formula becomes simplified and can be written as follows:

$$\Delta G_{\text{H}^*} = \Delta E_{\text{H}^*} + 0.24. \quad (12)$$

In accordance with Sabatier's principle [50], an effective and optimal catalytic activity of the HER can be characterized as a thermally neutral hydrogen binding on the materials, indicated by the  $\Delta G_{\text{H}^*}$  close to the zero value [51, 52]. Furthermore, the HER catalyst material with negative values of  $\Delta G_{\text{H}^*}$  implies that the reaction kinetics of H<sub>2</sub> release is relatively low, and the HER catalyst with a positive value leads to a rather low kinetic of hydrogen adsorption. Initially, the binding free energy of H-atom adsorbed at the most stable site on the considered monolayers was explored and depicted in figures 9(a)–(d). Based on our study, different adsorption sites are identified and explored for H-adsorbed on the surface of Al<sub>2</sub>XY (X ≠ Y|X, Y = S, Se, Te) monolayers. Figures 9(a)–(c) illustrate the full optimized structures of the most stable site of H-adsorbed on the Al<sub>2</sub>SSe, Al<sub>2</sub>STe, Al<sub>2</sub>SeTe systems, respectively. One can clearly notice that the hydrogen atom prefers to be adsorbed relatively on the hollow site bonded to Al atoms in the three considered systems. Also, figure 9(d) illustrates the corresponding calculated Gibbs free energy  $\Delta G_{\text{H}^*}$  for the three considered systems. Based on our results, the HER activity of Al<sub>2</sub>STe material is more significant than that of Al<sub>2</sub>SSe and Al<sub>2</sub>SeTe systems with a Gibbs free energy of about  $\Delta G_{\text{H}^*} = 1.15$  eV for Al<sub>2</sub>STe which is slightly lower than those of Al<sub>2</sub>SSe and Al<sub>2</sub>SeTe monolayers with a Gibbs free energy of approximately 1.28 eV. The Gibbs free energy found within

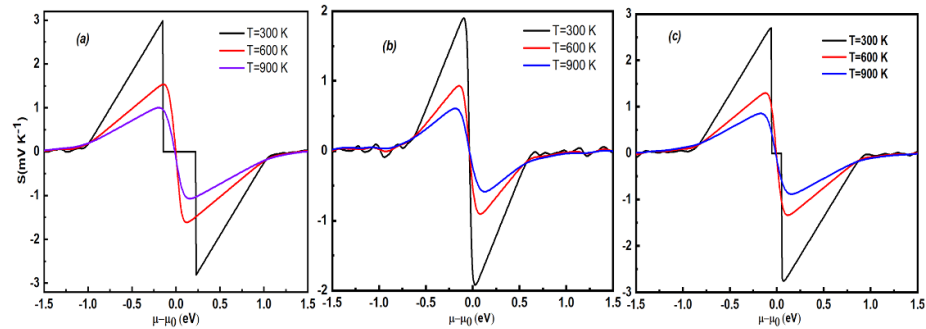


**Figure 10.** The computed Seebeck coefficient of the 2D Janus (a)  $\text{Al}_2\text{SSe}$ , (b)  $\text{Al}_2\text{STe}$ , and (c)  $\text{Al}_2\text{SeTe}$  monolayers depending on the charge carrier concentration at different temperatures.

this work are either higher or comparable to many other 2D materials recently reported such as Janus Gallium monochalcogenide monolayers  $\text{Ga}_2\text{SSe}$  ( $X \neq Y|X$ ,  $Y = \text{S, Se, Te}$ ) with Gibbs free energy ranging between 1.55 and 2.31 eV [53].

### 3.5. Thermoelectric transport properties of 2D Janus $\text{Al}_2\text{XY}$ monolayers

In this section, we will discuss thermoelectric transport properties of 2D Janus  $\text{Al}_2\text{XY}$  ( $X \neq Y|X$ ,  $Y = \text{S, Se, Te}$ ) materials by taking into consideration the relaxation-time constant approximation through the semi-classical Boltzmann approach. In this framework, we calculate and evaluate the relaxation time-dependent parameters such as the electrical conductivity ( $\sigma/\tau$ ) and the electronic part of the thermal conductivity ( $K_e/\tau$ ). Since chemical potential plays an important role in equilibrium chemistry, this is a reason to explore the thermoelectric properties of  $\text{Al}_2\text{XY}$  as a function of chemical potential. The positive chemical potentials reflect n-type doping with an upward shift of the Fermi level, while the negative chemical potentials reflect p-type doping with a downward shift of the Fermi level. The Seebeck coefficient versus the chemical potential at selected temperatures ( $T = 300, 600$ , and  $900$  K) is shown in figure 10. Accordingly, the highest values of the Seebeck coefficient are derived for chemical potentials ranging around the Fermi level. Above this interval, the curves tend towards 0. The highest Seebeck coefficient values are  $2981.2 \mu\text{V K}^{-1}$  ( $2807.7 \mu\text{V K}^{-1}$ ),  $2693.4 \mu\text{V K}^{-1}$  ( $2772.3 \mu\text{V K}^{-1}$ ), and  $1900.9 \mu\text{V K}^{-1}$  ( $1916.5 \mu\text{V K}^{-1}$ ) for  $\text{Al}_2\text{SSe}$ ,  $\text{Al}_2\text{SeTe}$ , and  $\text{Al}_2\text{STe}$ , respectively, at room temperature for p-type (n-type) dope. The negative value indicates that electrons are spread from the hot extremity to the cold one, making the cold extremity slightly more electron-concentrated than the hot one. As one can see from the figures, the values of the Seebeck coefficients diminish as the temperature rises due to the increase in a hole and electron conductivities caused by thermal energy. The Seebeck coefficients of  $\text{Al}_2\text{XY}$  exhibit higher values compared to pristine  $\text{AlX}$ . For instance, the Seebeck coefficient ( $S$ ) for n-type  $\text{AlS}$  is measured at  $322.89 \mu\text{V K}^{-1}$  (at 300 K). Similarly, other well-known thermoelectric materials such as  $\text{SiAs}$ ,  $\text{SiSb}$ ,  $\text{SiBi}$ , phosphorus, among others, also demonstrate noteworthy Seebeck coefficients [20, 54–56].

The electrical conductivity versus the chemical potential for the three temperatures is depicted in figures 11(a)–(c). Within the range of  $-0.5$ – $0.5$  eV, the value of electrical conductivity appears to be zero. However, beyond this interval, the electrical conductivity values increase with chemical potential. Furthermore, the changes in electrical conductivity with chemical potential are similar at different temperatures. Figures 11(d)–(f) displays the electronic thermal conductivity variation as a function of chemical potential at different temperatures. From these curves, it is evident that increasing the chemical potential and temperatures improve electronic thermal conductivity. The power factor is one of the most important parameters influencing the thermoelectric performance of the materials. The power factor variations as a function of chemical potential at the various temperatures are depicted in figures 12(a)–(c). For n-doping at 900 K, the high-power factor value is reached, i.e.  $2.7 \times 10^{11} \text{ W (m s K}^2)^{-1}$ ,  $2.85 \times 10^{11} \text{ W (m s K}^2)^{-1}$ , and  $3.1 \times 10^{11} \text{ W (m s K}^2)^{-1}$  for  $\text{Al}_2\text{SSe}$ ,  $\text{Al}_2\text{STe}$ , and  $\text{Al}_2\text{SeTe}$  respectively. Our analysis of the different transport coefficients ultimately led to the computation of the electronic thermoelectric figure of merit of  $\text{Al}_2\text{XY}$ . Figures 12(d)–(f) represents the variation of  $ZT$  as a function of chemical potential for different temperatures. In each system, two apparent peaks are observed in the vicinity of the Fermi level. The high values of  $ZT$  up to one for all three systems are observed. An exception is  $\text{Al}_2\text{STe}$  for which  $ZT$  is as high as 1.03 for the p-type. Therefore, the high  $ZT$  values of  $\text{Al}_2\text{XY}$  make them attractive candidates for thermoelectric applications.



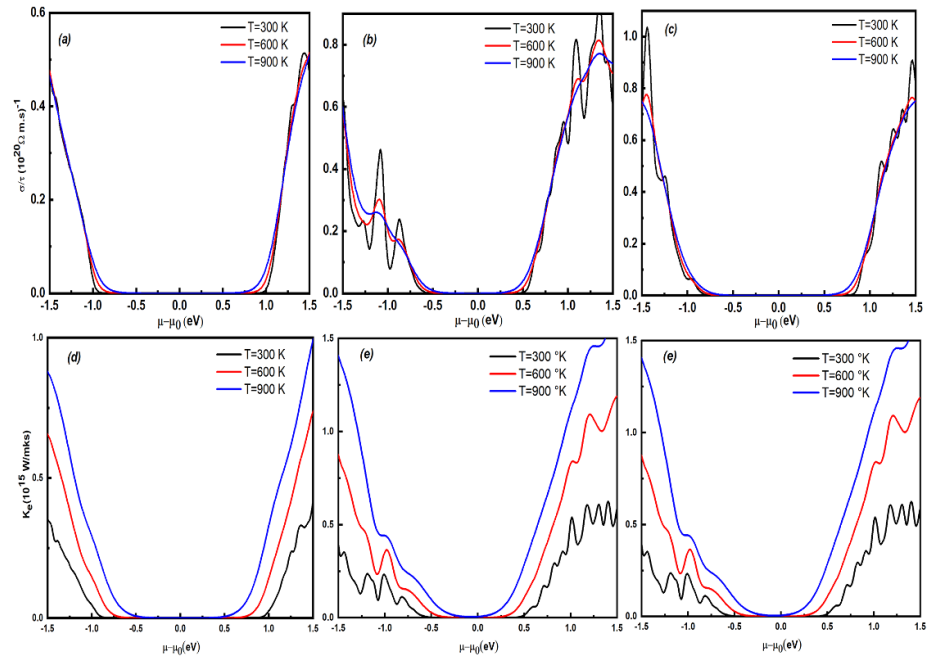


**Figure 11.** (a)–(c) The calculated electrical conductivity ( $\sigma/\tau$ ) and (d)–(f) electronic thermal conductivity ( $K_e/\tau$ ) of  $\text{Al}_2\text{SSe}$ ,  $\text{Al}_2\text{STe}$ , and  $\text{Al}_2\text{SeTe}$ , respectively.

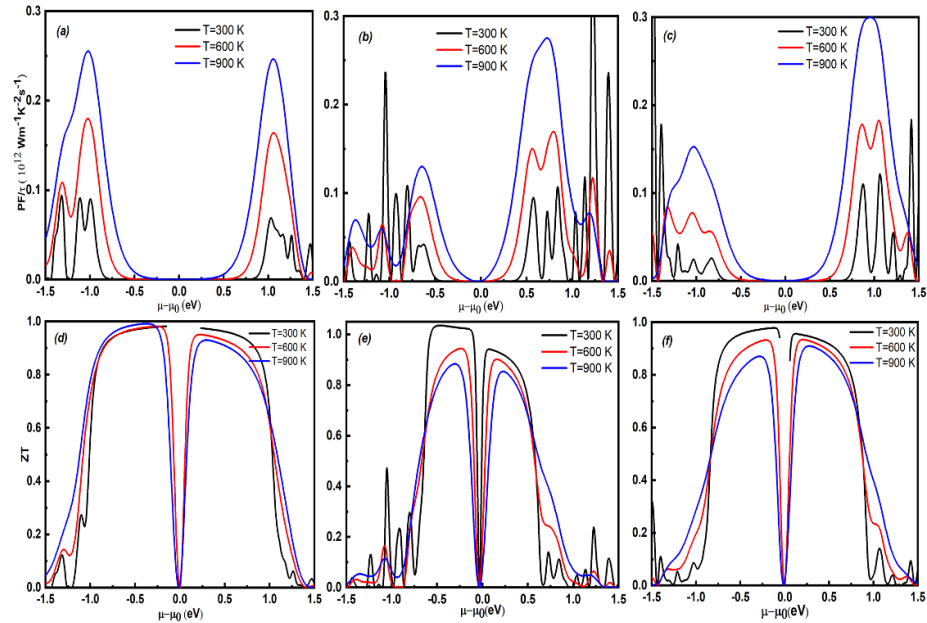


**Figure 12.** (a)–(c) The calculated power factors (PFs) and (d)–(f) figure of merits ZT of the three considered  $\text{Al}_2\text{SSe}$ ,  $\text{Al}_2\text{STe}$ , and  $\text{Al}_2\text{SeTe}$  monolayers, respectively.

## 4. Conclusion

We have carried out in-depth comprehensive studies of the structural, electronic, and optical properties of the 2D Janus aluminum monochalcogenide  $\text{Al}_2\text{XY}$  ( $X \neq Y$ ,  $X, Y = \text{S, Se, Te}$ ) monolayers as well as their possible use as a promising and efficient medium for photocatalytic and thermoelectric applications by means of *ab-initio* molecular dynamics and first principle calculations based on DFT. To begin with, our findings confirm the dynamical and thermal stability of the considered structures, showing the promising prospect of experimental realization of these materials. Besides, we established that the 2D Janus  $\text{Al}_2\text{SSe}$ ,  $\text{Al}_2\text{STe}$ , and  $\text{Al}_2\text{SeTe}$  monolayers show a semiconducting nature with indirect gaps of about 2.799, 1.823, and 2.348 eV obtained respectively through the HSE06 hybrid functional, which induces systems to absorb light



at varying frequency modes. Additionally, based on the computed valence and conduction band edge positions versus the redox potentials of water, it is found that the  $\text{Al}_2\text{XY}$  monolayers provide good photocatalytic activities, and could be implemented as catalysts for hydrogen production. The computed thermoelectric transport properties show a great efficiency of  $\text{Al}_2\text{XY}$  monolayers owing to the obtained wide figure of merit values. Furthermore, the thermoelectric transport parameters are observed to improve significantly as a function of temperature from 300 to 900 K. Finally, our outcomes not only provide information on the high dynamical and thermal stability of 2D Janus aluminum monochalcogenide materials in ultra-thin reflectors and absorbers for optoelectronic based technologies but provides a useful insight into the identification of new features for photocatalytic and thermoelectric based technologies, as well as proposing a new approach for the implementation of a wide range of light emission/detection and processing capabilities in selected frequency modes.

### Data availability statement

The data cannot be made publicly available upon publication because they are not available in a format that is sufficiently accessible or reusable by other researchers. The data that support the findings of this study are available upon reasonable request from the authors.

### Acknowledgments

The authors gratefully acknowledge computational resources from Moulay Ismail University. N K and P D acknowledge Dutch Research Council (NWO) Domain Science for the use of supercomputer facilities. R A acknowledge Swedish Research Council (VR-2016-06014 & VR-2020-04410) and J Gust. Richert Stiftelse, Sweden (2021-00665) for financial support and SNIC (2021/1-42 and 2022/1-34) Sweden for computer time. A A acknowledges the PPR2 Project (MESRSCI-CNRST).

### CRedit authorship contribution statement

**Zakarya Haman:** formal analysis, validation, writing—review & editing. **Moussa Kibbou:** formal analysis, visualization, validation, writing—review & editing. **Nabil Khossossi:** conceptualization, data curation, methodology, formal analysis, validation, visualization, writing—review & editing. **Soukaina Bahti:** formal analysis, validation, review & editing. **Poulumi Dey:** formal analysis, validation, review & editing. **Ismail Essaoudi:** formal analysis, validation, review & editing. **Rajeev Ahuja:** formal analysis, validation, review & editing. **Abdelmajid Ainane:** funding acquisition, project administration, resources, software, supervision, validation, review & editing.

### Conflict of interest

The authors declare that they have no known competing financial interests or personal relationships that could have appeared to influence the work reported in this paper.

### ORCID iDs

Nabil Khossossi  <https://orcid.org/0000-0002-3914-4162>

Ismail Essaoudi  <https://orcid.org/0000-0002-8043-6351>

Rajeev Ahuja  <https://orcid.org/0000-0003-1231-9994>

### References

- [1] Yu Y-J, Zhao Y, Ryu S, Brus L E, Kim K S and Kim P 2009 Tuning the graphene work function by electric field effect *Nano Lett.* **9** 3430–4
- [2] Pearson R J, Eisaman M D, Turner J W, Edwards P P, Jiang Z, Kuznetsov V L, Littau K A, Di Marco L and Taylor S G 2011 Energy storage via carbon-neutral fuels made from  $\text{CO}_2$ , water, and renewable energy *Proc. IEEE* **100** 440–60
- [3] Haman Z, Khossossi N, Kibbou M, Bouziani I, Singh D, Essaoudi I, Ainane A and Ahuja R 2022 Janus aluminum oxysulfide  $\text{Al}_2\text{OS}$ : a promising 2D direct semiconductor photocatalyst with strong visible light harvesting *Appl. Surf. Sci.* **589** 152997
- [4] Khossossi N, Luo W, Haman Z, Singh D, Essaoudi I, Ainane A and Ahuja R 2022 Revealing the superlative electrochemical properties of o- $\text{B}_2\text{N}_2$  monolayer in lithium/sodium-ion batteries *Nano Energy* **96** 107066
- [5] Naseri M, Salahub D R, Vu T V and Zakaryae H 2022  $\text{XSnS}_3$  ( $\text{X} = \text{Ga}, \text{In}$ ) monolayer semiconductors as photo-catalysts for water splitting: a first principles study *J. Mater. Chem.* **10** 11412–23
- [6] Seh Z W, Kibsgaard J, Dickens C F, Chorkendorff I, Nørskov J K and Jaramillo T F 2017 Combining theory and experiment in electrocatalysis: insights into materials design *Science* **355** eaad4998

- [7] Zheng Y, Jiao Y, Zhu Y, Li L H, Han Y, Chen Y, Du A, Jaroniec M and Qiao S Z 2014 Hydrogen evolution by a metal-free electrocatalyst *Nat. Commun.* **5** 1–8
- [8] Bouziani I, Kibbou M, Haman Z, Khossossi N, Essaoudi I, Ainane A and Ahuja R 2021 Two-dimensional Janus  $\text{Sn}_2\text{SSe}$  and  $\text{SnGeS}_2$  semiconductors as strong absorber candidates for photovoltaic solar cells: first principles computations *Physica E* **134** 114900
- [9] Nandi P, Rawat A, Ahammed R, Jena N and De Sarkar A 2021 Group-IV (A) Janus dichalcogenide monolayers and their interfaces straddle gigantic shear and in-plane piezoelectricity *Nanoscale* **13** 5460–78
- [10] Ju L, Bie M, Tang X, Shang J and Kou L 2020 Janus  $\text{WSSe}$  monolayer: an excellent photocatalyst for overall water splitting *ACS Appl. Mater. Interfaces* **12** 29335–43
- [11] Cai H, Gu Y, Lin Y-C, Yu Y, Geoghegan D B and Xiao K 2019 Synthesis and emerging properties of 2D layered III–VI metal chalcogenides *Appl. Phys. Rev.* **6** 041312
- [12] Demirtas M, Ozdemir B, Mogulkoc Y and Durgun E 2020 Oxygenation of monolayer gallium monochalcogenides: design of two-dimensional ternary  $\text{Ga}_2\text{XO}$  structures ( $\text{X} = \text{S}, \text{Se}, \text{Te}$ ) *Phys. Rev. B* **101** 075423
- [13] Cui Y, Peng L, Sun L, Qian Q and Huang Y 2018 Two-dimensional few-layer group-III metal monochalcogenides as effective photocatalysts for overall water splitting in the visible range *J. Mater. Chem. A* **6** 22768–77
- [14] da Silva R, Barbosa R, Mancano R R, Duraes N, Pontes R B, Miwa R, Fazzio A and Padilha J E 2019 Metal chalcogenides Janus monolayers for efficient hydrogen generation by photocatalytic water splitting *ACS Appl. Nano Mater.* **2** 890–7
- [15] Demirtas M, Varjovi M J, Çiçek M M and Durgun E 2020 Tuning structural and electronic properties of two-dimensional aluminum monochalcogenides: prediction of Janus  $\text{Al}_2\text{XX}'(\text{X}/\text{X}': \text{O}, \text{S}, \text{Se}, \text{Te})$  monolayers *Phys. Rev. Mater.* **4** 114003
- [16] Patel A, Singh D, Sonvane Y, Thakor P and Ahuja R 2020 High thermoelectric performance in two-dimensional Janus monolayer material  $\text{WS-X}$  ( $\text{X} = \text{S}$  and  $\text{Te}$ ) *ACS Appl. Mater. Interfaces* **12** 46212–9
- [17] Chaurasiya R, Tyagi S, Singh N, Auluck S and Dixit A 2021 Enhancing thermoelectric properties of Janus  $\text{WSSe}$  monolayer by inducing strain mediated valley degeneracy *J. Alloys Compd.* **855** 157304
- [18] Zhou S, Liu C-C, Zhao J and Yao Y 2018 Monolayer group-III monochalcogenides by oxygen functionalization: a promising class of two-dimensional topological insulators *npj Quantum Mater.* **3** 1–7
- [19] Demirci S, Avazl N, Durgun E and Cahangirov S 2017 Structural and electronic properties of monolayer group III monochalcogenides *Phys. Rev. B* **95** 115409
- [20] Chen X, Huang Y, Liu J, Yuan H and Chen H 2019 Thermoelectric performance of two-dimensional  $\text{AlX}$  ( $\text{X} = \text{S}, \text{Se}, \text{Te}$ ): a first-principles-based transport study *ACS Omega* **4** 17773–81
- [21] Guo Y, Zhou S, Bai Y and Zhao J 2017 Enhanced piezoelectric effect in Janus group-III chalcogenide monolayers *Appl. Phys. Lett.* **110** 163102
- [22] Jena N et al 2018 Emergence of high piezoelectricity along with robust electron mobility in Janus structures in semiconducting group IVB dichalcogenide monolayers *J. Mater. Chem. A* **6** 24885–98
- [23] Chen Y, Liu J, Yu J, Guo Y and Sun Q 2019 Symmetry-breaking induced large piezoelectricity in Janus tellurene materials *Phys. Chem. Chem. Phys.* **21** 1207–16
- [24] Kandemir A and Sahin H 2018 Janus single layers of  $\text{In}_2\text{SSe}$ : a first-principles study *Phys. Rev. B* **97** 155410
- [25] Haman Z, Khossossi N, Kibbou M, Bouziani I, Singh D, Essaoudi I, Ainane A and Ahuja R 2021 Computational identification of efficient 2D aluminium chalcogenides monolayers for optoelectronics and photocatalysts applications *Appl. Surf. Sci.* **556** 149561
- [26] Vu T V, Vi V T, Phuc H V, Nguyen C V, Poklonski N, Duque C, Rai D, Hoi B D and Hieu N N 2021 Electronic, optical and thermoelectric properties of Janus in-based monochalcogenides *J. Phys.: Condens. Matter* **33** 225503
- [27] Kresse G and Furthmüller J 1996 Efficient iterative schemes for ab initio total-energy calculations using a plane-wave basis set *Phys. Rev. B* **54** 11169
- [28] Perdew J P, Burke K and Ernzerhof M 1996 Generalized gradient approximation made simple *Phys. Rev. Lett.* **77** 3865
- [29] Heyd J, Scuseria G E and Ernzerhof M 2003 Hybrid functionals based on a screened coulomb potential *J. Chem. Phys.* **118** 8207–15
- [30] Monkhorst H J and Pack J D 1976 Special points for Brillouin-zone integrations *Phys. Rev. B* **13** 5188
- [31] Henkelman G, Arnaldsson A and Jónsson H 2006 A fast and robust algorithm for Bader decomposition of charge density *Comput. Mater. Sci.* **36** 354–60
- [32] Chaput L, Togo A, Tanaka I and Hug G 2011 Phonon-phonon interactions in transition metals *Phys. Rev. B* **84** 094302
- [33] Parlinski K, Li Z and Kawazoe Y 1997 First-principles determination of the soft mode in cubic  $\text{ZrO}_2$  *Phys. Rev. Lett.* **78** 4063
- [34] Togo A, Oba F and Tanaka I 2008 First-principles calculations of the ferroelastic transition between rutile-type and  $\text{CaCl}_2$ -type  $\text{SiO}_2$  at high pressures *Phys. Rev. B* **78** 134106
- [35] Singh D, Panda P K, Khossossi N, Mishra Y K, Ainane A and Ahuja R 2020 Impact of edge structures on interfacial interactions and efficient visible-light photocatalytic activity of metal–semiconductor hybrid 2D materials *Catal. Sci. Technol.* **10** 3279–89
- [36] Singh D, Khossossi N, Ainane A and Ahuja R 2020 Modulation of 2D  $\text{GaS}/\text{BTe}$  vdW heterostructure as an efficient her catalyst under external electric field influence *Catal. Today* **370** 14–25
- [37] Wooten F 2013 *Optical Properties of Solids* (New York: Academic)
- [38] Kibbou M, Haman Z, Bouziani I, Khossossi N, Benhouria Y, Essaoudi I, Ainane A and Ahuja R 2021  $\text{Cs}_2\text{InGaX}_6$  ( $\text{X} = \text{Cl}, \text{Br}, \text{I}$ ): emergent inorganic halide double perovskites with enhanced optoelectronic characteristics *Curr. Appl. Phys.* **21** 50–57
- [39] Kibbou M, Haman Z, Essaoudi I and Ainane A 2023 Designing new halide double perovskite materials  $\text{Rb}_2\text{AgGaX}_6$  ( $\text{X}: \text{Br}, \text{Cl}$ ) with direct band gaps and high power conversion efficiency *J. Solid State Chem.* **317** 123698
- [40] Dong J, Zhang B, Zhang S, Sun Y and Long M 2022 Effects of interface charge-transfer doping on thermoelectric transport properties of black phosphorene- $\text{F}_4\text{TCNQ}$  nanoscale devices *Appl. Surf. Sci.* **579** 152155
- [41] Cheng L-Y, Zhang K-C, Li Y-F, Liu Y and Zhu Y 2022 Thickness-dependent thermoelectric transporting properties of few-layered  $\text{SnSe}$  *J. Alloys Compd.* **894** 162542
- [42] Phuc H V, Tuan V V, Hieu N N, Ilyasov V V, Fedorov I A, Hoi B D, Phuong L T, Hieu N V, Feddi E and Nguyen C V 2018 Tuning the electronic and optical properties of two-dimensional graphene-like  $\text{C}_2\text{N}$  nanosheet by strain engineering *J. Electron. Mater.* **47** 4594–603
- [43] Choi S, Shaolin Z and Yang W 2014 Layer-number-dependent work function of  $\text{MoS}_2$  nanoflakes *J. Korean Phys. Soc.* **64** 1550–5
- [44] Lin C-Y, Ulaganathan R K, Sankar R and Chou F-C 2017 Ambipolar field-effect transistors by few-layer  $\text{InSe}$  with asymmetry contact metals *AIP Adv.* **7** 075314
- [45] Mouhat F and Coudert F-X 2014 Necessary and sufficient elastic stability conditions in various crystal systems *Phys. Rev. B* **90** 224104
- [46] Lee C, Wei X, Kysar J W and Hone J 2008 Measurement of the elastic properties and intrinsic strength of monolayer graphene *Science* **321** 385–8

- [47] Bui H D, Jappor H R and Hieu N N 2019 Tunable optical and electronic properties of Janus monolayers Ga<sub>2</sub>SSe, Ga<sub>2</sub>STe and Ge<sub>2</sub>SeTe as promising candidates for ultraviolet photodetectors applications *Superlattices Microstruct.* **125** 1–7
- [48] Haman Z, Kibbou M, Bouziani I, Benhouria Y, Essaoudi I, Ainane A and Ahuja R 2021 Structural, electronic and optical properties of two-dimensional Janus transition metal oxides MXO (M = Ti, Hf and Zr; X = S and Se) for photovoltaic and opto-electronic applications *Physica B* **604** 412621
- [49] Singh D, Khossossi N, Ainane A and Ahuja R 2021 Modulation of 2D GaS/BTe vdW heterostructure as an efficient her catalyst under external electric field influence *Catal. Today* **370** 14–25
- [50] Sabatier P 1911 Hydrogénations et déshydrogénations par catalyse *Ber. Dtsch. Chem. Ges.* **44** 1984–2001
- [51] Nørskov J K, Bligaard T, Logadottir A, Kitchin J, Chen J G, Pandalov S and Stimming U 2005 Trends in the exchange current for hydrogen evolution *J. Electrochem. Soc.* **152** J23
- [52] Khossossi N, Banerjee A and Dey P 2023 Synergistic effect of Fe/Co-doping and electric field in niobium diboride for boosting hydrogen production *Surf. Interfaces* **39** 102972
- [53] Cui Y, Li M, Zhang X, Wang S and Huang Y 2021 Ga<sub>2</sub>OSe monolayer: a promising hydrogen evolution photocatalyst screened from two-dimensional gallium chalcogenides and the derived Janus *Green Energy Env.* **7** 1045–52
- [54] Somaiya R N, Sonvane Y A and Gupta S K 2020 Exploration of the strain and thermoelectric properties of hexagonal six (X = N, P, As, Sb and Bi) monolayers *Phys. Chem. Chem. Phys.* **22** 3990–8
- [55] Kibbou M, Haman Z, Khossossi N, Essaoudi I, Ainane A and Ahuja R 2023 Computational insights into the superior efficiency of Cs<sub>2</sub>AgGa(Cl,Br)<sub>6</sub> double halide perovskite solar cells *Mater. Chem. Phys.* **294** 126978
- [56] Kibbou M, Haman Z, Khossossi N, Singh D, Essaoudi I, Ainane A and Ahuja R 2022 Probing the electronic, optical and transport properties of halide double perovskites Rb<sub>2</sub>InSb(Cl, Br)<sub>6</sub> for solar cells and thermoelectric applications *J. Solid State Chem.* **312** 123262